

Valence transition in topological Kondo insulator

Jia-Tao Zhuang,¹ Xiao-Jun Zheng,¹ Zhi-Yong Wang,¹ Xing Ming,¹ Huan Li,^{1,*} Yu Liu,^{2,3,†} and Hai-Feng Song^{2,3}

¹College of Science, Guilin University of Technology, Guilin 541004, China

²Institute of Applied Physics and Computational Mathematics, Beijing 100088, China

³Software Center for High Performance Numerical Simulation,
China Academy of Engineering Physics, Beijing 100088, China

(Dated: August 5, 2019)

We investigate the valence transition in three-dimensional topological Kondo insulator through slave-boson analysis of periodic Anderson model. By including the effect of intra-atomic Coulomb correlation U_{fc} between conduction and local electrons, we find a first-order valence transition from Kondo region to mixed valence upon ascending of local level above a critical U_{fc} , and this valence transition usually occurs very close to or simultaneously with a topological transition. Near the parameter region of zero-temperature valence transition, rise of temperature can generate a thermal valence transition from mixed valence to Kondo region, accompanied by a first-order topological transition. Remarkably, above a critical U_{fc} which is considerable smaller than that generating paramagnetic valence transition, the original continuous antiferromagnetic transition is shifted to first order one, at which a discontinuous valence shift takes place. Upon increased U_{fc} , the paramagnetic valence transition approaches with the first-order antiferromagnetic transition, leaving an significant valence shift on the magnetic boundary. The continuous antiferromagnetic transition, first-order antiferromagnetic transition, paramagnetic valence transition and topological transitions are all summarized in a global phase diagram. Our proposed exotic transition processes can help to understand the thermal valence variation as well as the valence shift around the pressure-induced magnetic transition in topological Kondo insulator candidates and in other heavy-fermion systems.

PACS numbers: 75.30.Mb, 75.70.Tj, 75.30.Kz

I. INTRODUCTION

Since the proposal of topological intrinsic in some special Kondo insulators (KI)^{1,2}, renewed attention has been attracted on these old materials, now are known as "topological Kondo insulators"(TKI) represented by SmB_6 ³⁻¹⁸. In these TKIs, the strong spin-orbit coupled hybridization between d and f electrons guarantees time-reversal symmetry (TRS) and generates a band inversion between d and f orbits at certain time-reversal-invariant momenta (TRIM), leading to a topologically protected state classified by Z_2 invariants^{1,2,4,19,20}. Via the spin- and angle-resolved photoemission spectroscopy (SARPES), the metallic surface states with Dirac points have been observed in SmB_6 , confirming its topological characteristic^{11,21}. A Variety of theoretical works have been carried out for TKI to reveal its rich topological phases, topological transitions, surface states, and magnetic transitions, through first-principle calculations as well as model calculations for periodic Anderson model (PAM)^{3,5-9,12,22-24}.

Recently, the high-pressure studies of SmB_6 demonstrate a magnetic transition at $6\sim 8$ GPa²⁵⁻³¹, around which the mean valence ν of Sm ion ($\text{Sm}^{\nu+}$) displays a quite rapid variation from 2.5 to saturated value 3³¹, in addition, the mean valence also increases as temperature rises^{32,33}, similar to other TKI candidates such as YbB_{12} and pressured golden SmS ³⁴⁻³⁶. In the hole representation for the f shell (in the filled $4f^6$ base) of Sm atom, the valence ν is related to the mean occupation of f holes n_f by $\nu = 2 + n_f$ ^{4,26}, so the valence shift of Sm ion indicates a variation of f -occupation with pressure, from mixed valence (MV), to Kondo region (or local moment region) in which the f electrons are nearly localized to create a magnetic order. In this context, the possible valence transi-

tion or valence crossover in TKI, as well as the relation to the magnetic transition deserve further theoretical investigation.

For Ce- and Yb- based heavy-fermion compounds, the first-order valence transition (FOVT) was observed decades ago in pressure studies³⁷⁻³⁹, in which the valences of Ce and Yb ion increase abruptly at a critical temperature, and under enhanced pressure, FOVT can be suppressed and terminates at a critical end point (CEP) to become a valence crossover. The valence of Ce (Yb) is manipulated by the electron (hole) occupation number n_f of the $4f$ shell⁴⁰, so the discontinuous valence jump indicates a first-order transition from MV (with small n_f) to Kondo region (nearly localized f electrons with $n_f \sim 1$). Pressure can drive magnetic transitions in some heavy-fermion compounds, and it's found that FOVT reaches the magnetic boundary (e.g. in YbInCu_4 ^{38,41}), implying a strong interplay between FOVT and magnetic transition. The zero-temperature FOVT in heavy-fermion systems can be understood through PAM by considering the on-site Coulomb repulsion U_{fc} between local f and conducting c electrons^{42,43}. Upon ascent of the energy level ϵ_f of f orbit by strengthened pressure, the influence of U_{fc} causes a much rapid ascent of the renormalized f level (relative to the chemical potential), pours the electrons into conduction band then consequently drives a decrease of f occupation number n_f , leading to the crossover behavior of the valence. Above a critical U_{fc} , the valence crossover is strengthened then finally changed into FOVT from Kondo region to MV, showing a abrupt fall of n_f at a critical ϵ_f ^{40,44}.

Beside ϵ_f , pressure applied on heavy-fermion compounds can lead to variations of other model parameters such as the hybridization strength, which all can affect the FOVT⁴⁰, so the experimentally observed FOVT is a combined outcome

within model description. In YbInCu₄, the enhanced pressure drives a FOVT from MV to Kondo region³⁸, contrary to Ce-based systems, therefore the pressure-induced FOVT cannot be simply attributed to the ascent of ϵ_f ⁴². By contrast, the FOVT from MV to Kondo region in Ce- and Yb- compounds by rising temperature is a purer effect thus can be interpreted more straightforwardly, but such thermal FOVT is still lacking of theoretical investigation. On the other hand, for SmB₆ and TKI candidate golden SmS, near the pressure-driven magnetic boundary, the valence of Sm ion shows an active increase^{30,31,45}, similarly, at low temperatures, the pressure-induced magnetic transition in YbInCu₄ holds simultaneously a FOVT³⁸, therefore, the relation of FOVT or valence crossover in TKI (and also in other heavy-fermion systems) to the magnetic transition should be clarified in an unified framework. Particularly, in TKI, variation of model parameters can produce various topological phases and distinct transition processes among them, and can driven magnetic transition as well^{46,47}, so interest questions arise, as how the FOVT or valence crossover appears in TKI? what is the relation between FOVT, topological transitions and magnetic transition? can any unrevealed novel transition process takes place in TKI?

This work is devoted to answer above questions. We first study the zero-temperature valence transition in three-dimensional TKI, modeling by spin-orbit coupled PAM with U_{fc} interactions. Similar to other typical KIs, we find the rise of f energy level ϵ_f can induce a rapid decrease of f electron number n_f , causing a valence crossover of f orbit, then above a critical U_{fc} , the valence crossover is shifted to a FOVT from Kondo region to MV. We also find that the U_{fc} interaction has an significant impact on the topological boundaries of TKI. Remarkably, FOVT generally takes place very close to a topological boundary, and with slightly greater U_{fc} than the critical one, FOVT can simultaneously cause a first-order topological transition, which should be clarified more rigorously in future studies. We also propose a thermal FOVT of TKI from MV to Kondo region by rising temperature in a narrow parameter regime, simultaneously with a first-order topological transition. Furthermore, we find the effect of U_{fc} interaction leads to a strong variation of f valence near the continuous antiferromagnetic (AF) transition in TKI, and further enhancement of U_{fc} can drive the AF transition from continuous one to first order one, meanwhile, the continuous valence variation is shifted to a FOVT at the AF boundary. In a narrow U_{fc} window, we find a gradual approaching then convergence between paramagnetic (PM) FOVT and FOVT-associated first-order AF transition on U_{fc} - ϵ_f plane. In addition, such FOVT-associated first-order AF transition can also be generated by increased temperature in some parameter regime. The PM FOVT, two classes of AF transitions and the topological transitions are all summarized in a global phase diagram.

Our work provides new insight into the exotic transition precesses in TKI, and can be used to qualitatively understand the observed thermal valence variation as well as the valence change around the magnetic transition in SmB₆, other TKIs and heavy-fermion systems.

TABLE I: Two sets of EHA used in this work

	t_d	t'_d	t''_d	t_f	t'_f	t''_f
EHA(I)	1	0.15	0	-0.2	-0.02	0
EHA(II)	1	-0.375	-0.375	-0.2	0.09	0.09

II. VALENCE TRANSITION AND TOPOLOGICAL TRANSITIONS

We use the spin-1/2 half-filled PAM in cubic lattice with a spin-orbit coupled c - f hybridization to describe TKI^{2,5}. This model is adopted frequently in the literature and successfully reveals the topological aspects of TKI^{6,12,46,48}. Besides, the on-site c - f Coulomb interaction U_{fc} is the crucial driving force of FOVT in heavy-fermion systems thus should be included^{40,42,44}. The model Hamiltonian of PAM reads:

$$\begin{aligned} \mathcal{H} = & \sum_{i,j,\sigma} (-t_{ij}^c c_{i\sigma}^\dagger c_{j\sigma} - t_{ij}^f f_{i\sigma}^\dagger f_{j\sigma}) + \epsilon_f \sum_{i,\sigma} f_{i\sigma}^\dagger f_{i\sigma} \\ & + U \sum_i n_{i\uparrow}^f n_{i\downarrow}^f - \left(\frac{iV}{2} \sum_{i,\vec{l},\alpha,\beta} \vec{l} \cdot \vec{\sigma}_{\alpha\beta} c_{i\alpha}^\dagger f_{i+\vec{l},\beta} + h.c.\right) \\ & + U_{fc} \sum_i n_i^c n_i^f - \mu \sum_{i,\sigma} (c_{i\sigma}^\dagger c_{i\sigma} + f_{i\sigma}^\dagger f_{i\sigma}), \end{aligned} \quad (1)$$

in which half-filling of total electrons $n_t = n_c + n_f = 2$ is fixed by adjusting the chemical potential μ , $\vec{\sigma}$ is three-dimensional vector formed by three Pauli matrices. We choose the electron hopping amplitude (EHA) up to next-next-nearest-neighbor, with the two sets of EHAs shown in Tab.I, both retaining an insulating bulk gap⁴⁶. The spin- and oriental- dependent hybridization between c and f electrons on neighboring sites linking by coordination vector \vec{l} guarantees the TRS of above PAM. The on-site f - f Coulomb repulsion U is general large thus is set to infinite for simplicity^{4,12,46,48}, appropriate for applying the standard slave-boson mean-field technique, through which we arrive at the effective Hamiltonian in momentum space as

$$\begin{aligned} H_{MF} = & N[\lambda(b^2 - 1) - U_{fc} n_c n_f] + \\ & \sum_{\mathbf{k},\alpha,\beta} (c_{\mathbf{k}\alpha}^\dagger, f_{\mathbf{k}\alpha}^\dagger) \begin{pmatrix} \tilde{\epsilon}_{\mathbf{k}}^c \delta_{\alpha\beta} & \tilde{V} \mathbf{S}_{\mathbf{k}} \cdot \vec{\sigma}_{\alpha\beta} \\ \tilde{V} \mathbf{S}_{\mathbf{k}} \cdot \vec{\sigma}_{\alpha\beta} & \tilde{\epsilon}_{\mathbf{k}}^f \delta_{\alpha\beta} \end{pmatrix} \begin{pmatrix} c_{\mathbf{k}\beta} \\ f_{\mathbf{k}\beta} \end{pmatrix}, \end{aligned} \quad (2)$$

in which α and β represent spin orientations, λ is the lagrange multiplier, b is the mean expectation value of slave bosons obeying the relation $n_f = 1 - b^2$. The effective hybridization is renormalized as $\tilde{V} = Vb$. U_{fc} term in Eq. 1 has been decoupled via Hatree-Fock approximation. The renormalized c and f dispersions are $\tilde{\epsilon}_{\mathbf{k}}^c = \epsilon_{\mathbf{k}}^c + U_{fc} n_f - \mu$ and $\tilde{\epsilon}_{\mathbf{k}}^f = b^2 \epsilon_{\mathbf{k}}^f + \epsilon_f + \lambda + U_{fc} n_c - \mu$, respectively, in which the tight-binding dispersions $\epsilon_{\mathbf{k}}^c$ and $\epsilon_{\mathbf{k}}^f$ are determined by their corresponding EHAs⁴⁶. $\mathbf{S}_{\mathbf{k}} = (\sin \mathbf{k} \cdot \mathbf{a}_1, \sin \mathbf{k} \cdot \mathbf{a}_2, \sin \mathbf{k} \cdot \mathbf{a}_3)$,¹² where $\mathbf{a}_1, \mathbf{a}_2, \mathbf{a}_3$ are the element vectors of cubic lattice.

The quasi-particle dispersions are derived by diagonalizing the Hamiltonian matrix in Eq.2 (in its modified form) as $E_{\mathbf{k}}^\pm = \frac{1}{2}[\tilde{\epsilon}_{\mathbf{k}}^c + \tilde{\epsilon}_{\mathbf{k}}^f \pm \sqrt{(\tilde{\epsilon}_{\mathbf{k}}^c - \tilde{\epsilon}_{\mathbf{k}}^f)^2 + 4\tilde{V}^2 S_{\mathbf{k}}^2}]$, both doubly degenerated, then the ground state energy is expressed by

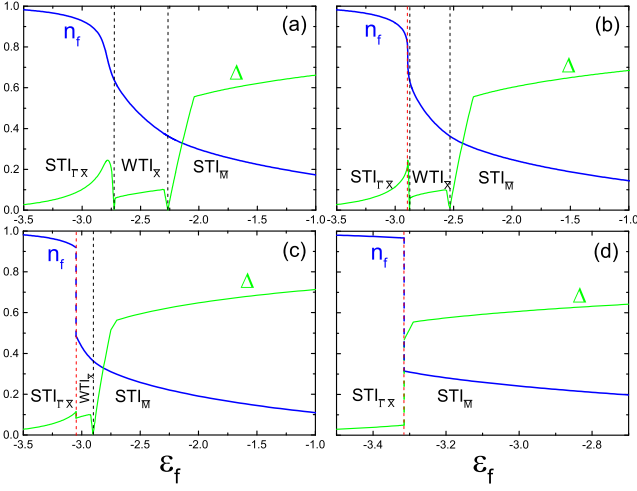


FIG. 1: (Color online) Occupation number of f orbit n_f and bulk insulating gap Δ as functions of local level ϵ_f . From (a) to (d), $U_{fc}=4.1, 4.31, 4.6, 5$. $U_{fc}=4.31$ is the critical value, above which a FOVT occurs at a certain ϵ_f , denoted by red dashed vertical lines. When U_{fc} is greater than 4.38, a first-order topological transition takes place simultaneously at FOVT ((c) and (d)). Black dashed vertical lines denote the conventional topological transitions. Parameters: EHA(II) and $V = 1$.

$E_g = N[\lambda(b^2 - 1) - U_{fc}n_c n_f] + 2 \sum_{\mathbf{k}, \pm} \theta(-E_{\mathbf{k}}^{\pm}) E_{\mathbf{k}}^{\pm}$. The mean-field parameters λ , b , and μ are then solved by saddle point approximation of E_g via $\partial E_g / \partial \mu = -n_t$, $\partial E_g / \partial \lambda = 0$ and $\partial E_g / \partial b = 0$, to obtain the following set of equations

$$\begin{aligned} n_t &= \frac{2}{N} \sum_{\mathbf{k}, \pm} \theta(-E_{\mathbf{k}}^{\pm}), \\ n_f &= \frac{1}{N} \sum_{\mathbf{k}, \pm} \theta(-E_{\mathbf{k}}^{\pm}) \left[1 \mp \frac{\tilde{\epsilon}_{\mathbf{k}}^c - \tilde{\epsilon}_{\mathbf{k}}^f}{\sqrt{(\tilde{\epsilon}_{\mathbf{k}}^c - \tilde{\epsilon}_{\mathbf{k}}^f)^2 + 4V^2 b^2 S_{\mathbf{k}}^2}} \right], \\ \lambda &= -\frac{1}{N} \sum_{\mathbf{k}, \pm} \theta(-E_{\mathbf{k}}^{\pm}) \left[\epsilon_{\mathbf{k}}^f \pm \frac{2V^2 S_{\mathbf{k}}^2 - \epsilon_{\mathbf{k}}^f (\tilde{\epsilon}_{\mathbf{k}}^c - \tilde{\epsilon}_{\mathbf{k}}^f)}{\sqrt{(\tilde{\epsilon}_{\mathbf{k}}^c - \tilde{\epsilon}_{\mathbf{k}}^f)^2 + 4V^2 b^2 S_{\mathbf{k}}^2}} \right], \end{aligned} \quad (3)$$

where $\theta(-E_{\mathbf{k}}^{\pm})$ is an step function. The above equations should be solved by numerical iteration.

In SmB_6 , the itinerant 5d band and local 4f band both locate near the Fermi level²², causing the emergence of intra-atomic Coulomb repulsion U_{fc} . Similarly, in Ce and Yb systems, such interactions are also non-ignorable and play a crucial role in their valence transitions, although the magnitude of U_{fc} may differs from each other⁴⁰. In this sense, the pressure- or temperature-induced valence variation of SmB_6 and other TKIs³¹⁻³⁶ should be understood on the basis of U_{fc} interaction. On the other hand, the pressure applied on heavy-fermion systems enhances the hybridization strength V , and elevates the local f level ϵ_f as well, therefore, to simulate the valence transition in TKI, we first test the valence change (embodied by variation of n_f) as a function of ϵ_f under various magnitudes of U_{fc} , then study the evolution of valence transition point with V .

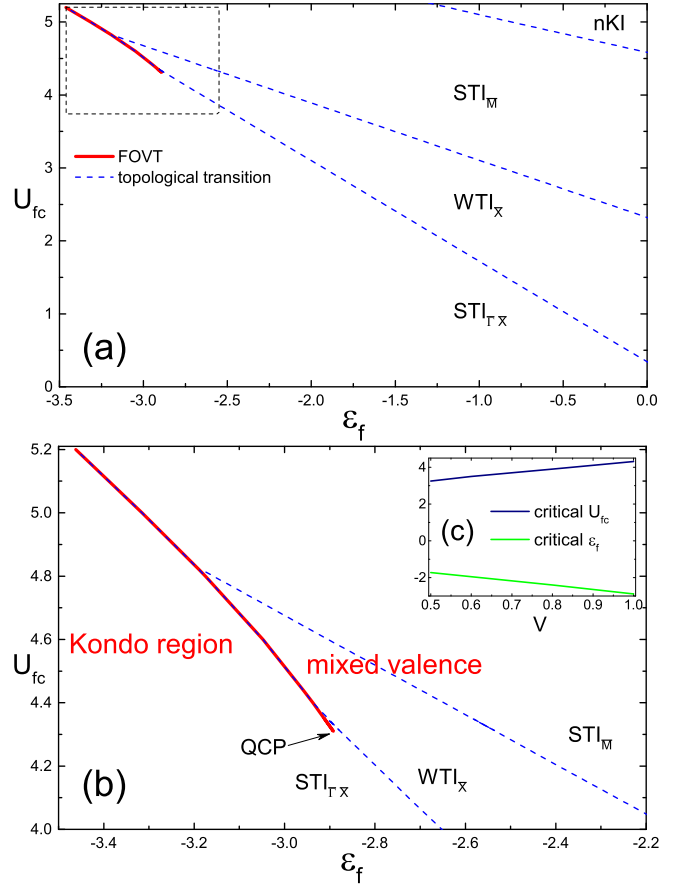


FIG. 2: (Color online) FOVT (red solid lines) driven by shift of local energy level ϵ_f at presence of c - f intra-atomic Coulomb interaction U_{fc} . Above a critical $U_{fc}=4.31$, a FOVT occurs between Kondo state ($n_f \sim 1$) and MV state (small n_f). Variation of U_{fc} also remarkably shifts the topological boundaries (blue dashed lines). (b) is a zoom in of the dashed area in (a). (c) illustrates the critical U_{fc} and ϵ_f of QCP as functions of hybridization V . Parameters: EHA(II); in (a) and (b), $V = 1$.

The numerical results are illustrated in Fig.1 with EHA(II) and $V = 1$. With weak U_{fc} , n_f decreases gradually with ascending ϵ_f , showing a valence crossover behavior, see Fig.1a. While U_{fc} is enhanced, n_f shows a stronger decline. At a critical value $U_{fc} = 4.31$, n_f drops sharply at $\epsilon_f = -2.89$, indicating the emergence of a quantum critical point (QCP), see Fig.1b. While U_{fc} is further increased, n_f shows an abrupt jump from $n_f \sim 1$ to $n_f \ll 1$ at a critical ϵ_f , generating a FOVT from Kondo region in which local moments weakly hybridize with c electrons, to MV region in which c and f electrons are strongly coupled, see Fig.1c-d. The FOVT is generated by strong U_{fc} interaction which forces the f electrons to pour into c band when the effective f level is suddenly lifted during the ascent of ϵ_f .

Previous works have shown that the variation of ϵ_f or V can produce successive topological transitions driven by closing and reopening of bulk insulating gap in TKI^{3,5,47}, and through present calculations, we find that these topological boundaries can be shifted sensitively by U_{fc} towards lower ϵ_f direction,

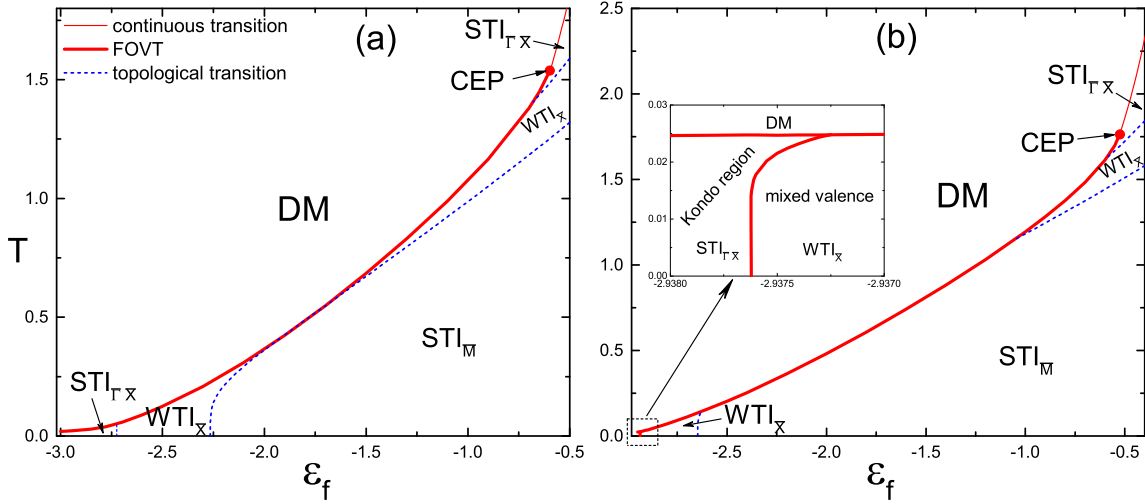


FIG. 3: (Color online) Phase diagram at non-zero temperatures for (a) $U_{fc} = 4.1$ and (b) $U_{fc} = 4.4$. Thick red lines denote FOVT, thin red lines denote continuous decoupling of heavy-fermion state, blue dashed lines denote topological transitions, red dots represent CEP of FOVT. Inset of (b) shows the thermal FOVTs among MV, Kondo and DM states. Parameters: EHA(II) and $V = 1$.

see the black dashed lines in Fig. 1a-c and blue dashed lines in Fig. 2. Remarkably, attributing to the rapid variation of bulk gap around the QCP of FOVT, the QCP usually locates very close to a certain topological transition, see Fig. 1b. Upon further increased U_{fc} from the QCP, the topological boundary first approaches then finally converges with FOVT, leaving a first-order topological transition characterized by discontinuous change of insulating gap. The unconventional first-order topological transition is a direct outcome of FOVT in TKI, and should be verified more rigorously in future work.

The QCP, FOVT and topological transitions are summarized on U_{fc} - ϵ_f plane from $U_{fc}=0$ in Fig. 2a. In Fig. 2b, the phase diagram around the QCP is shown in enlarged pattern, in which the FOVT successively converges with the topological boundaries at two points, one at $U_{fc}=4.38$ and $\epsilon_f=-2.93$, the other at $U_{fc}=4.82$ and $\epsilon_f=-3.19$, separating the FOVT into three segments: (1) when $4.31 < U_{fc} < 4.38$, FOVT occurs near conventional $STI_{\Gamma\bar{X}}$ - $WTI_{\bar{X}}$ transition (the subscripts denote the Dirac points on the surface Brillouin zone⁴⁷); (2) when $4.38 < U_{fc} < 4.82$, FOVT occurs simultaneously with first-order $STI_{\Gamma\bar{X}}$ - $WTI_{\bar{X}}$ transition; (3) when $U_{fc} > 4.82$, a first-order $STI_{\Gamma\bar{X}}$ - $STI_{\bar{M}}$ transition takes place at FOVT. Below the QCP, namely when $U_{fc} < 4.31$, U_{fc} is insufficient to produce FOVT, but rather a valence crossover between Kondo region and MV. Therefore, whether a heavy-fermion system undergoes a FOVT mainly depends on the strength of U_{fc} , e.g., in SmB₆ and SmS, the pressure- and temperature- induced valence shift in PM phase seem like a crossover behavior³⁰⁻³², which may imply a weak U_{fc} . It is also found that the critical U_{fc} of QCP mainly depends on the hybridization strength V . Due to the enhanced coherence between localized and itinerant electrons upon the increase of V , stronger U_{fc} is required to develop a QCP of valence transition, and the critical ϵ_f is pushed to deeper direction, see Fig. 2c.

III. THERMAL VALENCE TRANSITIONS

The ground-state FOVT discussed in above section may be experimentally realizable through external pressure, e.g. in Ce and Yb systems³⁷⁻³⁹, however, the alteration of external factors will lead to a series of changes for model parameters in PAM which are hard to track, hence it is difficult to compare above theoretical results with experiments. Therefore, in this section, we turn to the possible valence transition caused by temperature variation in TKI, which can be more clearly interpreted theoretically. Such "thermal valence transition" has been detected in Ce and Yb systems decades ago, in which the increase of temperature causes a FOVT from MV to Kondo state^{37,39,40}, but the mechanism and transition process of thermal valence transition are still lacking of theoretical verification. In SmB₆ and TKI candidates such as golden SmS, YbB₆ and YbB₁₂, the valences of Sm and Yb both increase with temperature at ambient pressure, and in some systems, the valence even reaches the saturated value^{30,32-36}, but it seems no discontinuous valence shift was observed in PM phase. We expect that the thermal valence behavior in TKI can be dramatically alternated under different magnitudes of pressure, since the pressure applied can affect the interaction strengths in heavy-fermion systems and lead to significant change of valence in the ground state^{30,31,34,36}.

At finite temperatures, the quasi-particle spectrums share the same formulas as those of the ground state, except that the mean-field parameters are now temperature-dependent, and are determined by the saddle-point equations derived from the free energy $F = N[\lambda(b^2 - 1) - U_{fc}n_c n_f] - 2T \sum_{\mathbf{k}, \pm} \ln(1 + e^{-E_{\mathbf{k}}^{\pm}/T})$ by $\partial F/\partial \mu = -n_t$, $\partial F/\partial \lambda = 0$ and $\partial F/\partial b = 0$, giving rise to the equation set the same as the ground state one (Eq. 3), except that now the step function $\theta(-E_{\mathbf{k}}^{\pm})$ should be replaced by Fermi distribution function $f_{\mathbf{k}}^{\pm} = 1/(1 + e^{E_{\mathbf{k}}^{\pm}/T})$ at non-zero temperatures.

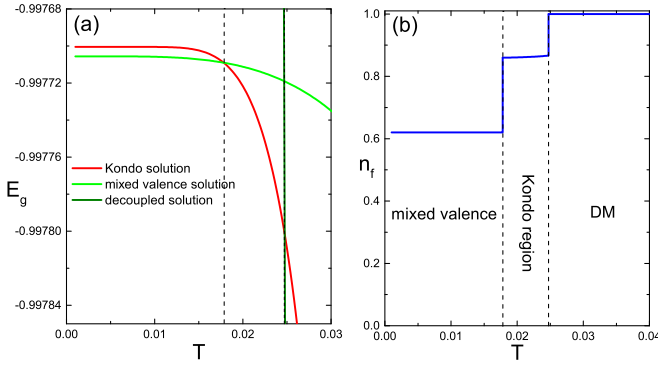


FIG. 4: (Color online) Thermal MV-Kondo and Kondo-DM FOVTs in the inset of Fig.3(b), with $\epsilon_f = -2.9376$. (a) Energy comparison of three solutions. (b) f -electron number n_f with increasing temperature, in which the dashed vertical lines denote two thermal FOVTs.

The T - ϵ_f phase diagrams are given in Fig.3a and 3b, with two magnitudes of $U_{fc} = 4.1$ and 4.4 , which are slightly smaller and greater than the QCP value $U_{fc} = 4.31$, respectively. As temperature increases, b is reduced gradually, but only when ϵ_f exceeds a certain value (-0.6 and -0.525 for $U_{fc} = 4.1, 4.4$, respectively), b (consequently \tilde{V}) gradually vanishes at a critical temperature, results in a second-order insulator-to-metal transition from heavy-fermion MV insulating state to a decoupled metallic state (DM) in which $n_f = 1$ with completely localized f electrons. Surprisingly, when ϵ_f is further reduced, the MV-DM transition becomes first-order, indicating a thermal FOVT, at which b and n_f undergo an abrupt jump to 0 and 1, respectively, Such discontinuous thermal decoupling of heavy-fermion state and MV-DM thermal FOVT accompanied by an insulator-metal transition deserves further verification.

Remarkably, when U_{fc} is greater than that of the QCP, we find that with ϵ_f slightly above that triggers the zero-temperature FOVT, there are two successive FOVTs with increasing temperature, first MV-to-Kondo FOVT, then Kondo-to-DM FOVT, see Fig.4, with the transition boundaries on T - ϵ_f plane shown in the inset of Fig.3b. Similar to zero-temperature case, the FOVT between MV and Kondo states also holds a first-order WTI $_{\bar{X}}$ -STI $_{\Gamma\bar{X}}$ topological transition. As ϵ_f rises, the Kondo region gradually shrinks, then two thermal FOVTs converge, leaving only a MV-DM transition. Moreover, with ϵ_f lower than that of zero-temperature FOVT, only Kondo-DM FOVT occurs with increased temperature. For U_{fc} less than the QCP value, no thermal MV-Kondo FOVT appears, since it is insufficient to support zero-temperature FOVT between MV and Kondo states.

In Ce systems, pressure can suppress the thermal FOVT, forces it to terminate at a CEP, leading to a thermal valence crossover behavior², this feature corresponds to a shift of thermal behavior from first-order to continuous one. In this sense, since pressure elevates ϵ_f , the ϵ_f -driven order change of thermal transitions may explain the appearance of CEP in Ce systems, which is marked by the red dots in Fig.3. In

contrast to Ce systems, for SmB₆ and TKI candidates SmS, YbB₆ and YbB₁₂, the Sm and Yb valences in PM phases seem to increase continuously with temperature^{30,32-36}, showing no clear signal of thermal FOVT. The absence of thermal FOVT in these TKIs may be ascribed to their weak U_{fc} interactions or their high f level ϵ_f which exceeds the CEP in Fig.3, leading to a continuous valence increase with temperature. Previous works suggested that magnetic field can shift the CEP of FOVT in Ce and Yb systems towards lower U_{fc} and higher ϵ_f ^{40,40}, similarly, we expect magnetic field can also shift the CEP of TKI to the right side on T - ϵ_f plane in Fig.3, and consequently recover a thermal FOVT in TKI under ambient pressure, which requires experimental verification.

IV. VALENCE VARIATION AROUND THE MAGNETIC TRANSITION

The high-pressure experiments of SmB₆ display a first-order transition to magnetically ordered state at $6\sim 8$ Gpa^{25,26}, around which the Sm valence shows a rapid increase³¹, afterwards, the Sm valence in the magnetic phase increases smoothly with pressure then approaches pure trivalent above 10 Gpa. For TKI candidate golden SmS³⁵, the pressure-induced magnetic transition at about 2 Gpa also exhibits first-order character⁴⁵, but around this transition, the valence increase of Sm in SmS is much sharper than in SmB₆³⁰. In YbInCu₄, with enhanced pressure, FOVT reaches the magnetic boundary at low temperatures^{38,41}, implying that the pressure-induced magnetic transition can hold a FOVT simultaneously. The active valence change at and around the magnetic transition indicates an intimate relation between these two transitions in TKI and in other heavy-fermion systems.

In order to study the valence variation around the magnetic transition in TKI, which is mostly likely an antiferromagnetic (AF) transition^{48,49}, we adopt Kotliar-Ruckenstein (K-R) slave-boson mean-field method⁵⁰⁻⁵³. This technique produces very close results of TKI to those of the conventional slave-boson approach, and has the advantage to include the magnetic order conveniently^{46,47}. The main feature of K-R representation for AF phase is that each f -creation and annihilation operator in c - f hybridization and f - f hopping is multiplied by a factor Z_+ or Z_- with $Z_{\pm} = \sqrt{\frac{2(1-n_f)}{2-n_f \mp m_f}}$, depending on the spin and sublattice of the f operator, in which m_f is the staggered magnetization of f electrons. Secondly, ϵ_f is shifted by a parameter η . Z_{\pm} and η are analogue to b and λ in conventional slave-boson method, respectively. The K-R mean-field treatment leads to the following effective Hamiltonian

$$\mathcal{H} = N(hm_f - \eta n_f - U_{fc} n_c n_f) + \sum_{\mathbf{k}} \Psi_{\mathbf{k}}^{\dagger} \mathbf{H}_{\mathbf{k}} \Psi_{\mathbf{k}}, \quad (4)$$

in which the summation of \mathbf{k} is restricted to the magnetic Brillouin zone (MBZ), h is a staggered parameter associated with m_f , $\Psi_{\mathbf{k}}^{\dagger} = (d_{\mathbf{k}A\uparrow}^{\dagger}, d_{\mathbf{k}A\downarrow}^{\dagger}, d_{\mathbf{k}B\uparrow}^{\dagger}, d_{\mathbf{k}B\downarrow}^{\dagger}, f_{\mathbf{k}A\uparrow}^{\dagger}, f_{\mathbf{k}A\downarrow}^{\dagger}, f_{\mathbf{k}B\uparrow}^{\dagger}, f_{\mathbf{k}B\downarrow}^{\dagger})$ is eight-component creation operator for c and f electrons in sublattice and spin spaces, the Hamiltonian matrix is given

by

$$\mathbf{H}_{\mathbf{k}} = \begin{pmatrix} \mathbf{H}_{\mathbf{k}}^d & \mathbf{V}_{\mathbf{k}} \\ \mathbf{V}_{\mathbf{k}}^\dagger & \mathbf{H}_{\mathbf{k}}^f \end{pmatrix}, \quad (5)$$

in which

$$\mathbf{V}_{\mathbf{k}} = V \begin{pmatrix} 0 & 0 & Z_- s_z & Z_+ \Gamma_{\mathbf{k}} \\ 0 & 0 & Z_- \Gamma_{\mathbf{k}}^* & -Z_+ s_z \\ Z_+ s_z & Z_- \Gamma_{\mathbf{k}} & 0 & 0 \\ Z_+ \Gamma_{\mathbf{k}}^* & -Z_- s_z & 0 & 0 \end{pmatrix} \quad (6)$$

hybridizes c and f electrons on neighboring sites.

$$\mathbf{H}_{\mathbf{k}}^d = \begin{pmatrix} (t'_c \gamma_{\mathbf{k}} + U_{fc} n_f - \mu) & u_{\mathbf{k}}^c \\ u_{\mathbf{k}}^c & (t'_c \gamma_{\mathbf{k}} + U_{fc} n_f - \mu) \end{pmatrix} \otimes I_2, \quad (7)$$

$$\mathbf{H}_{\mathbf{k}}^f = \begin{pmatrix} e_{\mathbf{k}}^+ & 0 & Z_+ Z_- u_{\mathbf{k}}^f & 0 \\ 0 & e_{\mathbf{k}}^- & 0 & Z_+ Z_- u_{\mathbf{k}}^f \\ Z_+ Z_- u_{\mathbf{k}}^f & 0 & e_{\mathbf{k}}^- & 0 \\ 0 & Z_+ Z_- u_{\mathbf{k}}^f & 0 & e_{\mathbf{k}}^+ \end{pmatrix}, \quad (8)$$

are the sublattice versions of tight-binding Hamiltonian for c and f , respectively, in which the f hopping amplitudes are renormalized by Z_{\pm} . I_2 is a two-order unit matrix, $\Gamma_{\mathbf{k}} = s_x - i s_y$, $\gamma_{\mathbf{k}} = -4(c_x c_y + c_x c_z + c_y c_z)$, $e_{\mathbf{k}}^{\pm} = \epsilon_f + \eta + U_{fc} n_c - \mu \mp h + t'_f Z_{\pm}^2 \gamma_{\mathbf{k}}$, $u_{\mathbf{k}}^{c(f)} = t_{c(f)} \lambda_{\mathbf{k}} + t''_{c(f)} g_{\mathbf{k}}$ with $\lambda_{\mathbf{k}} = -2(c_x + c_y + c_z)$ and $g_{\mathbf{k}} = -8c_x c_y c_z$, where we denote $c_i = \cos k_i$ and $s_i = \sin k_i$ ($i = x, y, z$) for simplicity.

The free energy can be expressed as the expectation value of the effective Hamiltonian by

$$F = N(h m_f - \eta n_f - U_{fc} n_c n_f + \mu n_t) + \sum_{\mathbf{k}, n, m} (\mathbf{H}_{\mathbf{k}})_{nm} \langle (\Psi_{\mathbf{k}}^\dagger)_n (\Psi_{\mathbf{k}})_m \rangle, \quad (9)$$

where subscripts n and m are row or column numbers. Use the unitary transformation matrix $\mathbf{U}_{\mathbf{k}}$ extracted from numerical diagonalization of $\mathbf{H}_{\mathbf{k}}$, we have

$$\langle (\Psi_{\mathbf{k}}^\dagger)_n (\Psi_{\mathbf{k}})_m \rangle = \sum_{i=1}^8 (\mathbf{U}_{\mathbf{k}})_{ni}^* (\mathbf{U}_{\mathbf{k}})_{mi} f_{\mathbf{k}}^{(i)}, \quad (10)$$

where $f_{\mathbf{k}}^{(i)} = 1/(1 + e^{E_{\mathbf{k}}^{(i)}/T})$ is the Fermi distribution of quasi-particles, and equals the step function $\theta(-E_{\mathbf{k}}^{(i)})$ at zero temperature. The set of equations determining the parameters n_f , m_f , h , η , μ can be obtained through the zero point of the derivation of free energy (Eq.9) with respect to them, by using the formulas of matrix elements $(\mathbf{H}_{\mathbf{k}})_{nm}$ in Eq.5⁴⁶.

In order to give a global phase diagram including both PM and AF phases through K-R solution, we also solve the K-R saddle-point equations for n_f , η and μ in PM phase, which

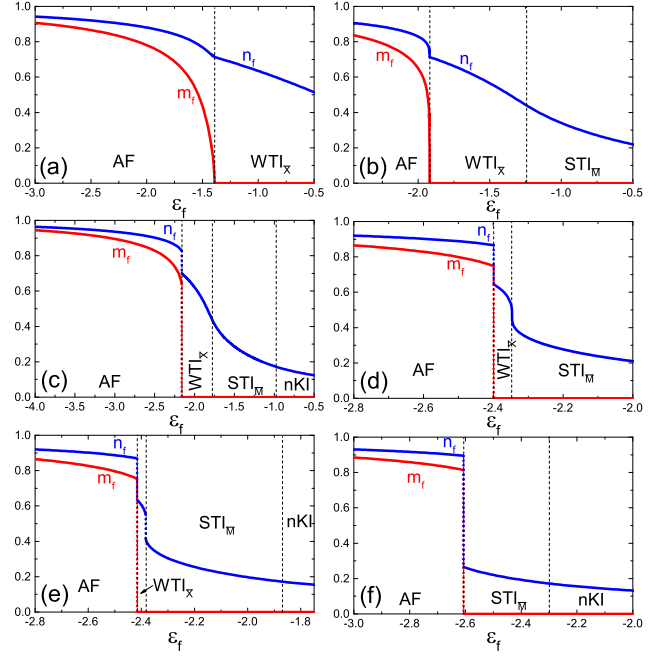


FIG. 5: (Color online) Staggered magnetization m_f and f -electron occupation n_f vs local level ϵ_f . Parameters: EHA(I), $V = 1$, and from (a) to (f), $U_{fc}=2, 2.92, 3.4, 3.906, 3.94, 4.2$. (a) and (b) show continuous AF transition without valence shift. For (c) and (d), the AF transition is shifted to first-order and is accompanied by a valence jump. For (e), the FOVT-associated AF transition and paramagnetic FOVT take place at different ϵ_f , while in (f), two transitions converge, leaving a FOVT-associated AF transition with significant valence jump.

are similar to those in section II and III:

$$\begin{aligned} n_t &= \frac{2}{N} \sum_{\mathbf{k}, \pm} f_{\mathbf{k}}^{\pm}, \\ n_f &= \frac{1}{N} \sum_{\mathbf{k}, \pm} f_{\mathbf{k}}^{\pm} \left[1 \mp \frac{\tilde{\epsilon}_{\mathbf{k}}^c - \tilde{\epsilon}_{\mathbf{k}}^f}{\sqrt{(\tilde{\epsilon}_{\mathbf{k}}^c - \tilde{\epsilon}_{\mathbf{k}}^f)^2 + 4V^2 Z^2 S_{\mathbf{k}}^2}} \right], \\ \eta &= \frac{2Z}{N} \frac{\partial Z}{\partial n_f} \sum_{\mathbf{k}, \pm} f_{\mathbf{k}}^{\pm} \left[\epsilon_{\mathbf{k}}^f \pm \frac{2V^2 S_{\mathbf{k}}^2 - \epsilon_{\mathbf{k}}^f (\tilde{\epsilon}_{\mathbf{k}}^c - \tilde{\epsilon}_{\mathbf{k}}^f)}{\sqrt{(\tilde{\epsilon}_{\mathbf{k}}^c - \tilde{\epsilon}_{\mathbf{k}}^f)^2 + 4V^2 Z^2 S_{\mathbf{k}}^2}} \right], \end{aligned} \quad (11)$$

in which $Z = \sqrt{\frac{2(1-n_f)}{2-n_f}}$, $\tilde{\epsilon}_{\mathbf{k}}^f = Z^2 \epsilon_{\mathbf{k}}^f + \epsilon_f + \eta + U_{fc} n_c - \mu$, $f_{\mathbf{k}}^{\pm} = 1/(1 + e^{E_{\mathbf{k}}^{\pm}/T})$ for finite temperatures and equals the step function $\theta(-E_{\mathbf{k}}^{\pm})$ at zero temperature, where $E_{\mathbf{k}}^{\pm} = \frac{1}{2}[\tilde{\epsilon}_{\mathbf{k}}^c + \tilde{\epsilon}_{\mathbf{k}}^f \pm \sqrt{(\tilde{\epsilon}_{\mathbf{k}}^c - \tilde{\epsilon}_{\mathbf{k}}^f)^2 + 4V^2 Z^2 S_{\mathbf{k}}^2}]$

We first study the zero-temperature phase diagram on U_{fc} - ϵ_f plane. For convenience, we choose EHA(I) in Tab.I, set various values of U_{fc} from zero, then calculate the corresponding evolution of m_f and n_f vs ϵ_f to locate the AF transitions. Above the AF boundaries, the evolution of PM phases is computed via Eq.11 to determine the FOVT and topological boundaries. The results are shown with increasing U_{fc} from Fig.5a to 5f. For small U_{fc} , m_f variation indicates an

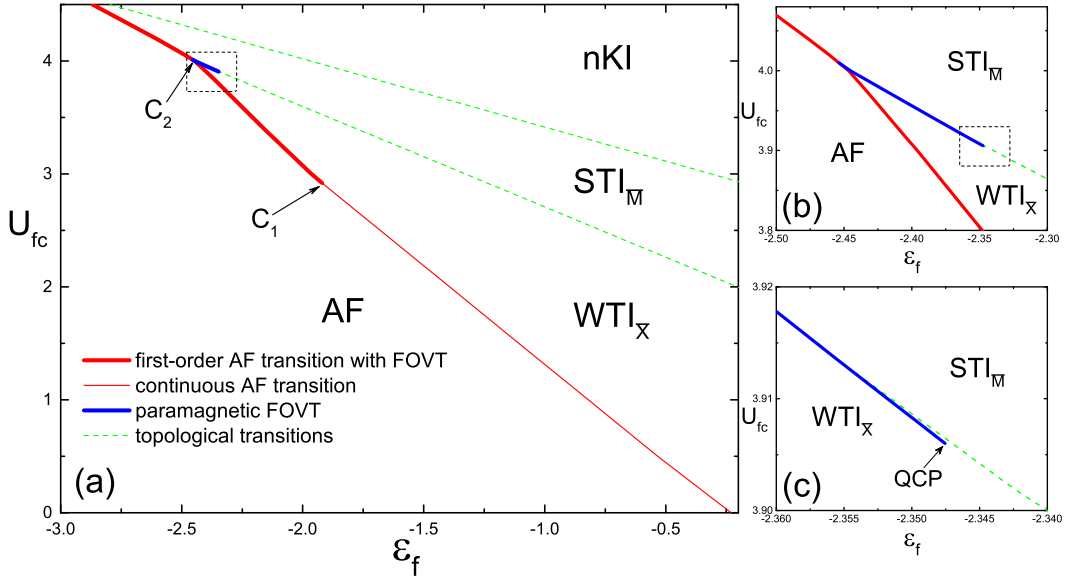


FIG. 6: (Color online) U_{fc} - ϵ_f magnetic phase diagram, showing the continuous AF transition (thin red line), first-order AF transition (thick red line) associating with a FOVT, and FOVT in PM phase (thick blue line). Topological transitions are denoted by dashed green lines. (b) and (c) are enlarged view of the dashed boxes in (a) and (b), respectively. Parameters: EHA(I), $V=1$.

second-order magnetic transition, at which n_f changes continuously with a kink; when U_{fc} exceeds 2.92, we find a first-order magnetic transition at which n_f shows an abrupt jump, indicating a FOVT-associated first-order AF transition; in the PM phase with ϵ_f above the first-order AF boundary, n_f decreases rapidly with ϵ_f , and when $U_{fc} > 3.906$ gives rise to a FOVT at a critical ϵ_f above the first-order AF transition; with further increased U_{fc} , the two transitions approach each other and then converge, leaving a large n_f jump at the first-order AF transition.

The resulting ground-state phase diagram on U_{fc} - ϵ_f plane is summarized in Fig.6, including the topological transitions in PM phase. In Fig.6a, it can be clearly seen that a critical point C_1 at $(U_{fc} = 2.92, \epsilon_f = -1.92)$ separates the AF boundaries into continuous part and first-order part, which is below and above C_1 , respectively. The FOVT in PM phase is denoted by blue solid lines in Fig.6a, and the enlarged view near the QCP at $(U_{fc} = 3.906, \epsilon_f = -2.348)$ is demonstrated in Fig.6c, in which the relative position between FOVT and topological boundaries behaves similarly to Fig.2b. Here we should point out that in K-R solution, the critical U_{fc} and ϵ_f for the QCP of FOVT in PM phase is slightly greater and lower than the conventional slave-boson solution, respectively, meanwhile the FOVT and topological transition processes in PM phase remain essential the same. The interplay between first-order AF transition and PM FOVT is clearly illustrated in Fig.6b: with increasing U_{fc} from QCP, the two boundaries approach each other and finally converge at C_2 ($U_{fc} = 4.01, \epsilon_f = -2.45$), leading to an single first-order AF boundary accompanied by a FOVT with significant valence jump. In addition, the coexistence of FOVT-associated AF transition and PM FOVT on ϵ_f axis only occurs in a narrow U_{fc} regime from 3.906 to 4.01. Therefore, the FOVT-associated first-order AF transitions are also classified into

two classes: one with weak valence shift below C_2 , and the other with strong valence jump above C_2 . Consequently, the order of AF transition, as well as the “strength” of first-order AF transition both depend on the magnitude of U_{fc} , in this sense, the weak first-order magnetic transitions in pressured SmB₆ and SmS may be ascribed to their relatively small d - f intra-atomic Coulomb repulsion as analysed in above sections^{25,26,45}, while the remarkable valence change at the magnetic transition in YbInCu₄ may be attributed to its stronger U_{fc} ^{38,41}. It is worth noting that the critical $U_{fc} = 2.92$ of C_1 which triggers a first-order AF transition is much smaller than that drives a FOVT in PM phase ($U_{fc} = 3.906$ of QCP), explaining why Sm valence varies continuously with temperature at ambient pressure in SmB₆ and SmS, meanwhile first-order AF transitions appear under high pressure.

Then we study the thermal phase transitions on T - ϵ_f plane, the results are displayed in Fig.7. For U_{fc} smaller than the critical point C_1 , the zero-temperature AF transition with ϵ_f is continuous, while ϵ_f descends, the thermal AF transition is shifted to first-order with valence jump (see Fig.7a), implying that the critical point C_1 separating these two types of AF transitions is temperature dependent and is pushed by increasing temperature towards lower ϵ_f and weaker U_{fc} . By comparison, for U_{fc} stronger than zero-temperature C_1 , thermal AF transition remains first-order, because U_{fc} keeps greater than C_1 when temperature rises. For temperature above the AF transitions, Z factor reduces with temperature, leading to the increase of n_f then finally a decoupling of heavy-fermion state to DM state with $n_f = 1$ at a critical temperature, giving rise to HF-DM transition. By contrast to AF transitions, the order of this HF-DM transition is only weakly temperature-dependent and mainly depends on U_{fc} : when U_{fc} is less or larger than zero-temperature C_1 in Fig.6a, HF-DM transition is continuous or first-order, respectively, and the latter coex-

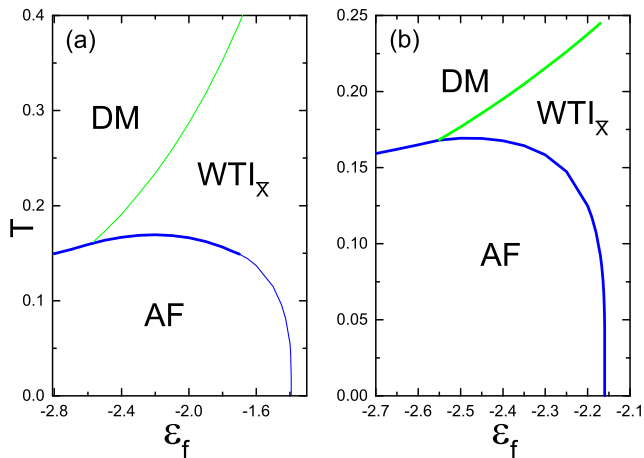


FIG. 7: (Color online) AF transitions (blue lines) and transitions between heavy-fermion state and DM state (green lines). Thin lines denote continuous transitions, while thick lines denote first-order transitions with valence shift. Parameter: EHA(I), $V = 1$. $U_{fc} = 2$ and 3.4 in (a) and (b), respectively.

ists a FOVT. As ϵ_f descends, the AF boundary and HF-DM boundary gradually converge, leaving a first-order AF-DM transition with abrupt valence shift. The thermal first-order AF transition coexisting a FOVT deserves more rigorous theoretical and experimental examinations.

V. CONCLUSION AND DISCUSSION

To summarize, we have proposed a series of exotic valence transition processes in TKI, driven by the effect of on-site Coulomb repulsion U_{fc} between conduction and local electrons in the PAM. For the ground state, we located a QCP on the U_{fc} - ϵ_f plane, above which a FOVT boundary separates the Kondo state with MV state, and holds an abrupt valence jump upon ascending ϵ_f . The QCP is very close to a topological transition, and the FOVT boundary gradually approaches then converges with the topological boundary, leading to a discontinuous topological transition. Near the parameter regime of the zero-temperature FOVT, increase in temperature can lead to a series of thermal FOVTs among the Kondo state, MV state and DM state. In addition, we found a CEP on T - ϵ_f plane which terminates the thermal FOVT

from heavy-fermion state to DM state, and shift the thermal decoupling of heavy-fermion state into continuous one under higher ϵ_f above the CEP. Further descent of ϵ_f can generate an AF order in TKI, and above a critical U_{fc} which is considerably smaller than that of the QCP which triggers a PM FOVT, the ϵ_f -driven continuous AF transition is shifted to first-order, accompanied by a FOVT. Further increasing of U_{fc} can push the first-order AF transition to approach then to join the PM FOVT boundary, giving rise to a first-order AF transition with large valence shift. The thermal AF transitions can also be classified into continuous one or first-order one, depending mainly on the magnitude of U_{fc} . The distinct valence-variation processes with temperature and pressure observed in TKI candidates SmB_6 , golden SmS and other heavy-fermion compounds, as well as their valence behaviors near the magnetic transitions can be qualitatively understood by our results in terms of their different magnitudes of U_{fc} . This work has used a simplified PAM with single conduction and f band to describe TKI, actually in real cubic TKI systems such as SmB_6 , dominant hybridization channel involves spin-degenerated $5d_{x^2-y^2}$, $5d_{3z^2-r^2}$ orbitals, and $\Gamma_8^{(1)}$, $\Gamma_8^{(2)}$ $4f$ quartet, resulting in much complicated tight-binding and hybridization terms^{4,7,54}. Although the multiple parameters can all influence the detailed valence-variation process in TKI, we believe that the intra-atomic Coulomb interaction U_{fc} between d and f orbitals still provides a crucial factor controlling the valence transition, and the magnitudes of U_{fc} in TKI candidates may be examined through first-principle simulations²².

Acknowledgments

H. Li is supported by NSFC (No. 11764010) and Guangxi Natural Science Foundation (No. 2017GXNSFAA198169). Y. Liu and H. F. Song thank the Science Challenge Project (Grant No. TZ2018002). Y. Liu is also supported by Open Research Fund Program of the State Key Laboratory of Low-Dimensional Quantum Physics (No. KF201702) and the SPC-Lab Research Fund (No. XKFZ201605). Z. Y. Wang is supported by NSFC (No. 11564008). X. J. Zheng is supported by NSFC (No. 11704084) and Guangxi NSF (No. 2017GXNSFBA198115). X. Ming is supported by NSFC (No. 11864008) and Guangxi NSF (No. 2018GXNSFAA138185).

* Electronic address: lihuan@glut.edu.cn

† Electronic address: liu_yu@iapcm.ac.cn

¹ Maxim Dzero, Kai Sun, Victor Galitski, and Piers Coleman, Phys. Rev. Lett. **104**, 106408 (2010).

² Maxim Dzero, Kai Sun, Piers Coleman, and Victor Galitski, Phys. Rev. B **85**, 045130 (2012).

³ Minh-Tien Tran, Tetsuya Takimoto, and Ki-Seok Kim, Phys. Rev. B **85**, 125128 (2012).

⁴ Victor Alexandrov, Maxim Dzero, and Piers Coleman, Phys. Rev.

Lett. **111**, 226403 (2013).

⁵ Markus Legner, Andreas Rüegg, and Manfred Sigrist, Phys. Rev. B **89**, 085110 (2014).

⁶ Jan Werner and Fakher F. Assaad, Phys. Rev. B **89**, 245119 (2014).

⁷ Bitan Roy, Jay D. Sau, Maxim Dzero, and Victor Galitski, Phys. Rev. B **90**, 155314 (2014).

⁸ Junwon Kim, Kyoo Kim, Chang-Jong Kang, Sooran Kim, Hong Chul Choi, J.-S. Kang, J. D. Denlinger, and B. I. Min, Phys. Rev.

- B **90**, 075131 (2014).
- ⁹ Pier Paolo Baruselli and Matthias Vojta, *Phys. Rev. B* **90**, 201106(R) (2014).
- ¹⁰ G. Li, Z. Xiang, F. Yu, T. Asaba, B. Lawson, P. Cai, C. Tinsman, A. Berkley, S. Wolgast, Y. S. Eo, Dae-Jeong Kim, C. Kurdak, J. W. Allen, K. Sun, X. H. Chen, Y. Y. Wang, Z. Fisk, Lu Li, *Science* **346**, 1208 (2014).
- ¹¹ N. Xu, P.K. Biswas, J.H. Dill, R.S. Dhaka, G. Landolt, S. Muff, C.E. Matt, X. Shi, N.C. Plumb, M. Radovic, E. Pomjakushina, K. Conder, A. Amato, S.V. Borisenko, R. Yu, H.-M. Weng, Z. Fang, X. Dai, J. Mesotl, H. Ding, and M. Shi, *Nat. Commun.* **5**, 4566 (2014).
- ¹² Victor Alexandrov, Piers Coleman, and Onur Erten, *Phys. Rev. Lett.* **114**, 177202 (2015).
- ¹³ Zhen Zheng, Xu-Bo Zou and Guang-Can Guo, *New J. Phys.* **20**, 023039 (2018).
- ¹⁴ Harris Pirie, Yu Liu, A. Soumyanarayanan, Pengcheng Chen, Yang He, M.M. Yee, P.F.S. Rosa, J.D. Thompson, Dae-Jeong Kim, Z. Fisk, Xiangfeng Wang, J. Paglione, Dirk K. Morr, M. H. Hamidian, and Jennifer E. Hoffman, arXiv:1810.13419v1.
- ¹⁵ Jianjun Ying, Lingyun Tang, Fei Chen, Xianhui Chen, and Viktor V. Struzhkin, *Phys. Rev. B* **97**, 121101(R) (2018).
- ¹⁶ J.J. van den Broeke, S.N. Kempkesy, A. Queller, X.F. Wang, J. Paglione, and C. Morais Smith, arXiv: 1803.03553v1.
- ¹⁷ Yoshiyuki Ohtsubo, Yuki Yamashita, Kenta Hagiwara, Shin-ichiro Ideta, Kiyohisa Tanaka, Ryu Yukawa, Koji Horiba, Hiroshi Kumigashira, Koji Miyamoto, Taichi Okuda, Wataru Hirano, Fumitoshi Iga, and Shin-ichi Kimura, arXiv:1803.09433v3.
- ¹⁸ W. T. Fuhrman, J. C. Leiner, J. W. Freeland, M. van Veenendaal, S. M. Koohpayeh, W. Adam Phelan, T. M. McQueen, and C. Broholm, *Phys. Rev. B* **97**, 121101(R) (2018).
- ¹⁹ Maxim Dzero and Victor Galitski, *J. Exp. Theor. Phys.* **117**, 499 (2013).
- ²⁰ Maxim Dzero, Jing Xia, Victor Galitski, and Piers Coleman, *Annu. Rev. Condens. Matter Phys.* **7** 249 (2016)
- ²¹ Nan Xu, Hong Ding, and Ming Shi, *J. Phys.: Condens. Matter* **28**, 363001 (2016).
- ²² Feng Lu, JianZhou Zhao, Hongming Weng, Zhong Fang, and Xi Dai, *Phys. Rev. Lett.* **110**, 096401 (2013).
- ²³ Rui Yu, Hongming Weng, XiaoHu, Zhong Fang, and Xi Dai, *New J. Phys.* **17**, 023012 (2015).
- ²⁴ Markus Legner, Andreas Rüegg, and Manfred Sigrist, *Phys. Rev. Lett.* **115**, 156405 (2015).
- ²⁵ A. Barla, J. Derr, J. P. Sanchez, B. Salce, G. Lapertot, B. P. Doyle, R. Rüffer, R. Lengsdorf, M. M. Abd-Elmeguid, and J. Flouquet, *Phys. Rev. Lett.* **94**, 166401 (2005).
- ²⁶ J. Derr, G. Knebel, G. Lapertot, B. Salce, M-A Méasson and J. Flouquet, *J. Phys.: Condens. Matter* **18**, 2089 (2006).
- ²⁷ J. Derr, G. Knebel, D. Braithwaite, B. Salce, J. Flouquet, K. Flachbart, S. Gabáni, and N. Shitsevalova, *Phys. Rev. B* **77**, 193107 (2008).
- ²⁸ Parisiades Paraskevas, Bremholm Martin, and Mezouar Mohamed, *Europhys. Letts.* **110**, 66002 (2015).
- ²⁹ N. Emi, N. Kawamura, M. Mizumaki, T. Koyama, N. Ishimatsu, G. Pristáš, T. Kagayama, K. Shimizu, Y. Osanai, F. Iga, and T. Mito, *Phys. Rev. B* **97**, 161116(R) (2018).
- ³⁰ Nicholas P. Butch, Johnpierre Paglione, Paul Chow, Yuming Xiao, Chris A. Marianetti, Corwin H. Booth, and Jason R. Jeffries, *Phys. Rev. Lett.* **116**, 156401 (2016).
- ³¹ Yazhou Zhou, Qi Wu, Priscila F. S. Rosa, Rong Yu, Jing Guo, Wei Yi, Shan Zhang, Zhe Wang, Honghong Wang, Shu Cai, Ke Yang, Aiguo Li, Zheng Jiang, Suo Zhang, Xiangjun Wei, Yuying Huang, Peijie Sun, Yi-feng Yang, Zachary Fisk, Qimao Si, Zhongxian Zhao, Liling Sun, *Science Bulletin* **62**, 1439 (2017).
- ³² Masaichiro Mizumaki, Satoshi Tsutsui, and Fumitoshi Iga, *J. Phys.: Conf. Ser.* **176**, 012034 (2009).
- ³³ Qi Wu and Liling Sun, *Rep. Prog. Phys.* **80** 112501 (2017).
- ³⁴ E. Annese, A. Barla, C. Dallera, G. Lapertot, J-P. Sanchez, and G. Vankó, *Phys. Rev. B* **73**, 140409(R) (2006).
- ³⁵ Zhi Li, Jin Li, Peter Blaha, and Nicholas Kioussis, *Phys. Rev. B* **89**, 121117 (2014).
- ³⁶ Kenta Hagiwara, Yusuke Takeno, Yoshiyuki Ohtsubo, Ryu Yukawa, Masaki Kobayashi, Koji Horiba, Hiroshi Kumigashira, Julien Rault, Patrick Le Fèvre, François Bertran, Amina Taleb-Ibrahimi, Fumitoshi Iga, Shin-ichi Kimura, *J. Phys.: Conf. Series* **807**, 012003 (2017).
- ³⁷ I. Felner and I. Nowik, *Phys. Rev. B* **33**, 617 (1985).
- ³⁸ T. Mito, T. Koyama, M. Shimoide, S. Wada, T. Muramatsu, T. C. Kobayashi, and J. L. Sarrao, *Phys. Rev. B* **67**, 224409 (2003).
- ³⁹ T. Park, V. A. Sidorov, J. L. Sarrao, and J. D. Thompson, *Phys. Rev. Lett.* **96**, 046405 (2006).
- ⁴⁰ Shinji Watanabe, Atsushi Tsuruta, Kazumasa Miyake, and Jacques Flouquet, *J. Phys. Soc. Jpn* **78**, 104706 (2009).
- ⁴¹ C. D. Immer, J. L. Sarrao, Z. Fisk, A. Lacerda, C. Mielke, and J. D. Thompson, *Phys. Rev. B* **56**, 71 (1997).
- ⁴² A. V. Goltsev and G. Bruls, *Phys. Rev. B* **63**, 155109 (2001).
- ⁴³ Shinji Watanabe, Masatoshi Imada, and Kazumasa Miyake, *J. Phys. Soc. Jpn* **75**, 043710 (2006).
- ⁴⁴ Shinji Watanabe, Atsushi Tsuruta, Kazumasa Miyake, and Jacques Flouquet, *Phys. Rev. Lett.* **100**, 236401 (2008).
- ⁴⁵ A. Barla, J. P. Sanchez, Y. Haga, G. Lapertot, B. P. Doyle, O. Leupold, R. Rüffer, M.M. Abd-Elmeguid, R. Lengsdorf, and J. Flouquet, *Phys. Rev. Lett.* **92**, 066401 (2004).
- ⁴⁶ Huan Li, Yin Zhong, Yu Liu, Hong-Gang Luo and Hai-Feng Song, *Journal of Physics: Condensed Matter* **30**, 435601 (2018).
- ⁴⁷ Huan Li, Zhi-Yong Wang, Xiao-Jun Zheng, Yu Liu and Yin Zhong, *Chin. Phys. Lett.* **35**, 127501 (2018).
- ⁴⁸ Robert Peters, Tsuneya Yoshida, and Norio Kawakami, *Phys. Rev. B* **98**, 075104 (2018).
- ⁴⁹ Kai-Wei Chang and Peng-Jen Chen, *Phys. Rev. B* **97**, 195145 (2018).
- ⁵⁰ Gabriel Kotliar and Andrei E. Ruckenstein, *Phys. Rev. Lett.* **57**, 1362 (1986).
- ⁵¹ Min-Fong Yang, Shih-Jye Sun, and Tzay-Ming Hong, *Phys. Rev. B* **48**, 16123 (1993).
- ⁵² Shih-Jye Sun, Min-Fong Yang, and Tzay-Ming Hong, *Phys. Rev. B* **48**, 16127 (1993).
- ⁵³ Shih-Jye Sun, Tzay-Ming Hong, Min Fong Yang, *Physica B* **216**, 111 (1995).
- ⁵⁴ Tetsuya Takimoto, *J. Phys. Soc. Jpn* **80**, 123710 (2011).